THE JOURNAL OF PHYSICAL CHEMISTRY C

pubs.acs.org/JPCC Article

NMR-Detected Host–Guest Proton Exchange as a Tool to Explore Surface/Volume Ratios and Fluid Filling of Internal and External Spaces of Porous Solids Containing Surface OH Groups

Verónica Torres-Barthelemy, Natalia Pérez-Hernández, Ilya G. Shenderovich,* Peter M. Tolstoy, Gleb S. Denisov, and Hans-Heinrich Limbach*

Cite This: *J. Phys. Chem. C* 2020, 124, 22082–22095 Read Online

ACCESS | Metrics & More | Article Recommendations | Supporting Information

ABSTRACT: A solid-state ^{1}H magic-angle spinning (MAS) NMR method is described to characterize the internal pore spaces and the external void spaces of powdered mesoporous solids containing surface OH groups. This method is based on fast proton exchange between homogeneously distributed surface OH groups of the porous hosts and added guests containing exchangeable NH protons. The position of the coalesced NH/OH signal in a given local space depends on its surface/volume ratio (S/V). In the case of slow guest exchange between spaces with different S/V ratios, coalesced signals are observed for each space where the relative signal intensities reflect the mole fractions of the guests in the different spaces. This method was tested by performing ^{1}H MAS NMR experiments on the samples of liquid 4-methyl-1*H*-pyrazole (MPz) embedded in mesoporous silica of the MCM-41 type (2.9 nm pore diameter) and the SBA-15 type (8.9 nm pore diameter). To guarantee fast NH/OH proton exchange, the experiments were performed at 398 K well below the boiling point. Three distinct signals were observed for MPz assigned to (i) the internal cylindrical pores, (ii) the external interstitial void space between the packed particles, and (iii) the space outside the powdered solid containing neat liquid MPz. From the NMR data analysis, surface/volume ratios are derived for the internal pores, which agree well with those obtained with a simple geometrical model after applying a surface-roughness correction. In addition, S/V ratios for the external space, as well as internal surface/external surface (S/S) and internal volume/external volume (V/V) ratios, are derived. It is shown that at low filling fractions, MPz preferentially enters the internal pores, but at larger fractions, MPz enters the external spaces. Moreover, it is shown that the final internal pore NH/OH ratio is achieved before the pores are filled. A scenario that rationalizes these findings in connection with the hydrogen-bonded states of MPz is presented where the number and the hydrogen-bonded state of guest molecules in a given pore are discussed.

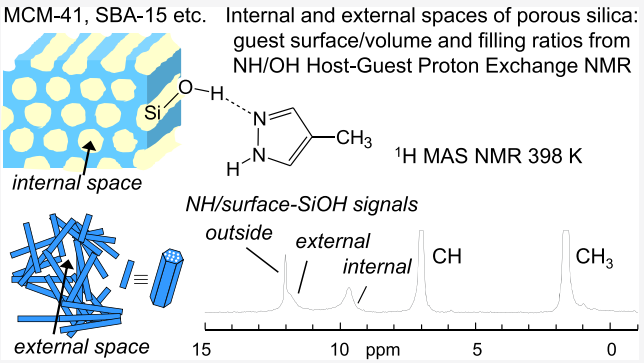

INTRODUCTION

Porous nano- or mesoscopic solids are of wide interest in science and technology.[1,2] They exhibit large surface areas in confined void spaces inside crystallites or particles, which can be filled with fluid guest molecules. Often, the materials consist of inorganic oxides such as silica-containing surface OH groups. The latter can serve as anchors for functional molecules or catalysts. Among the main properties of such materials are their specific pore surface areas S and pore volumes V per weight, which are generally determined using the Brunauer–Emmet–Teller (BET) technique.[3] In the latter, the N_2 gas adsorption isotherms at 77 K are measured as a function of pressure. It is assumed that the density of the adsorbed nitrogen is the same as in the liquid state and, hence, the "ruler" used to explore surfaces and volumes is of molecular dimensions. It is possible to determine S and V separately for internal and external spaces by methods based on adsorption isotherm measurements and comparison with reference materials,[4] by Hg-intrusion porosimetry[5] and by He-pycnometry.[6] Last but not least, pulsed-field gradient (PFG) NMR techniques have been used to study diffusion and transport of fluids in porous systems from which structural features such as S/V ratios can also be derived.[7−9] However, the interest is focused on meso- to macroscopic dimensions, leading to S/V ratios, which differ from those obtained in the molecular scale. For example, S/V ratios of porous rocks measured using PFG NMR of water as fluid were between 9 and 85 times smaller than those obtained by BET techniques.[8]

Received: May 30, 2020
Revised: August 28, 2020
Published: September 11, 2020

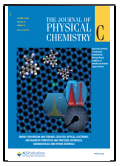

This is because the PFG NMR measurements do not detect the fine roughness of the surfaces that exhibit fractal properties.

Here, we describe an NMR method applicable to molecular dimensions to obtain further information not only about S/V ratios of porous solids but also about the number and location of guest molecules in the latter as a function of the guest filling fraction. This method is applicable to materials containing surface OH groups or other groups containing exchangeable protons. Generally, the number of surface OH groups of porous oxides is proportional to the surface area. Fluid heterocyclic molecules are used as guest molecules, which exhibit exchangeable NH groups.

For such systems, we show that the guest molecule/surface-OH ratios $R = N_{NH}/N_{OH}$ can be obtained by the solid-state ^{1}H NMR from which S/V ratios can be derived. This method requires fast host−guest proton exchange (HGPE) between the guest NH groups and the surface OH groups. In this case, an average NH/OH signal is observed by ^{1}H NMR, exhibiting a characteristic chemical shift from which R can be derived. R is very sensitive to the shape and the size of the confined space containing the guest and can therefore be different for internal pores and external spaces. R can also provide information about the pore filling processes of both environments.

After searching for a suitable fluid molecular guest and NMR marker, we chose 4-methyl-1*H*-pyrazole (MPz),[10] whose chemical structure is shown in Scheme 1. Pyrazoles contain

Scheme 1. Chemical Structure of 4-Methyl-1*H*-pyrazole (MPz, Fomepizole)

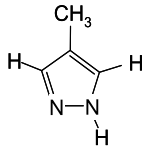

exchangeable NH protons and can form hydrogen-bonded linear and cyclic self-associates subjected to various kinds of proton exchange in the liquid and the solid state.[11−14] In contrast to other pyrazoles, MPz is liquid at room temperature so that it can be easily loaded into porous materials. Its boiling point is 477 K[10] and, hence, weight losses due to evaporation are small. MPz constitutes a drug, which is also called "fomepizole", as it is an inhibitor of alcohol dehydrogenase.[15] At 100 K, MPz forms cyclic H-bonded trimers as found by X-ray crystallography.[16]

As we were interested in porous SiO_2 materials, which are often used as excipients for drug delivery,[17,18] we have developed and applied the HGPE technique to the study of ordered mesoporous silicas of the MCM-41[19] and SBA-15 types.[20] These materials have been the subjects of an increasing number of studies of structure and dynamics, as well as applications, in particular after the introduction of functional groups.[21−30] According to X-ray diffraction, neutron scattering, and electron microscopy,[31−35] MCM-41 and SBA-15 form hexagonal crystallites (Figure 1a), where each one constitutes arrays of approximately hexagonally arranged cylindrical pores of uniform size disposed parallel to each other and separated by thin walls (Figure 1b). The pore diameters of MCM-41 range between 2 and 7 nm and of SBA-15 between 5 and 15 nm. The dimensions of the silica materials studied here, obtained from Findenegg et al.'s group, are illustrated in Figure 1.[35] We note that the materials may

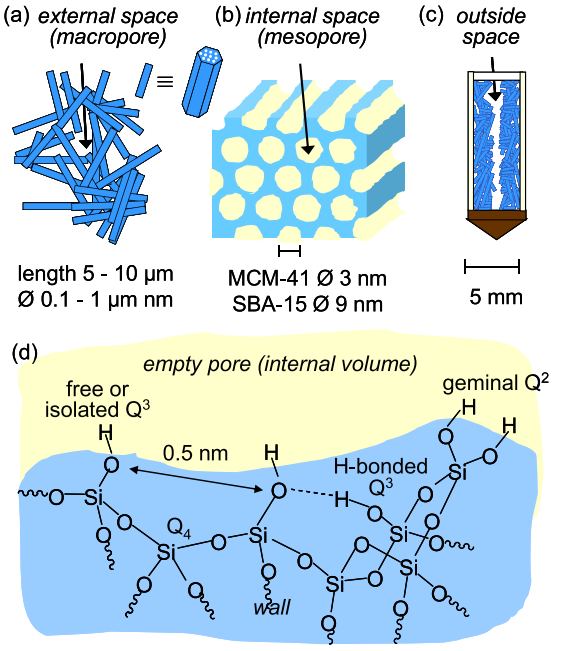

Figure 1. (a) Crystalline powder of mesoporous silica consisting of hexagonally shaped crystallites. The arrow indicates the external or interstitial space between crystallites. (b) Cylindrical ordered mesopores of a given crystallite. The arrow indicates the volume of an internal pore. (c) Rotor filled with mesoporous silica powder for magic-angle spinning (MAS) NMR experiments. The centrifugal forces compress the crystallites somewhat toward the rotor walls and create an axial void space outside the powder, as illustrated by the arrow. (d) Model of an inner pore wall according to ref 41. Different types of exchangeable surface protons are depicted: single SiOH groups of the Q^3 type and geminal $Si(OH)_2$ groups (Q^2 type). Both types can form hydrogen bonds with added guest molecules in the internal pores or form hydrogen bonds within the walls. The dimensions were taken from ref 35.

exhibit small pore deformations after filling with molecular guests.[36−38] Some properties of the materials studied in this work are assembled in Table 1.

Table 1. Structural Properties of the MCM-41 and SBA-15 Materials Studied

		MCM-41	SBA-15
pore ordering (X-ray diffraction electron microscopy[35])		hexagonal arrays	
surface silanol groups (NMR[39])		isolated SiOH uniformly distributed	isolated, hidden, interacting SiOH, geminal $Si(OH)_2$
pore-to-pore distance (X-ray diffraction[35])	a_0	4.0 nm	11.1 nm
pore diameter (N_2 adsorption[35])	d	2.9 nm	8.9 nm
wall thickness (X-ray diffraction, electron microscopy,[35] NMR[40])	$a_0 - d$	1 nm	2 nm
specific surface area (BET[35])	S^{BET}	1180 $m^2\ g^{-1}$	750 $m^2\ g^{-1}$
specific pore volume (BET[35])	V^{BET}	0.79 $cm^3\ g^{-1}$	1.06 $cm^3\ g^{-1}$
surface/volume ratio (BET)	S^{BET}/V^{BET}	1.495 nm^{-1}	0.7075 nm^{-1}
surface silanol groups per surface area (NMR[39])	n_{SiOH}	3 nm^{-2}	3.7 nm^{-2}

https://dx.doi.org/10.1021/acs.jpcc.0c04889
J. Phys. Chem. C 2020, 124, 22082−22095

The internal pore surface is very large in comparison with the external surface of the crystallites and has usually been neglected. Moreover, little is known about the external volumes, which might depend on the way how the crystallites are compacted. In solid-state NMR experiments, which employ magic-angle sample spinning (MAS), there is a third possibility for the location of an added liquid guest in a rotor, as illustrated in Figure 1c. Crystallites are displaced toward the rotor walls by centrifugal forces and lead to a void space around the rotor axis. We label this space or macropores as outside. When mesoporous silica materials containing catalytic centers are embedded in colloidal solutions for catalyzing chemical reactions, the external and the outer space coincide.

The atomic structure of mesoporous silica has been explored using multinuclear high-resolution solid-state NMR of the neat[42−44] and filled or functionalized materials.[39,41,68,45−57] In particular, signal enhancement using the dynamic nuclear polarization (DNP) method has been proposed.[58−60] These studies have revealed that mesoporous silica exhibits surface Si atoms of the Q^4, Q^3, or Q^2 type containing either no, one, or two (geminal) SiOH groups, as depicted in Figure 1d. MCM-41 exhibits mostly isolated surface OH groups of the Q^3 type, 3 per nm^2, about 0.5 nm away from each other (Table 1). They can all form hydrogen bonds with pyridine, as revealed by solid-state NMR.[39] An anisotropic motion of pyridine while jumping from one SiOH group to the next one indicates a small surface roughness. By contrast, SBA-15 type exhibits very rough inner surfaces, which have been modeled in terms of surface complexes reaching into the pore center.[39]

In the following, after the Experimental Section, we describe the results of ^{1}H MAS NMR experiments performed at 398 K on MPz embedded in MCM-41 and SBA-15. This temperature is well below the boiling point so that MPz molecules in the gas phase do not need to be considered in the data analyses. MCM-41 and SBA-15 have pore diameters of 2.9 and 8.9 nm, respectively.[35] The MPz/silica weight/weight filling ratios were varied in a wide range.

By analysis of the spectra, we obtained information about the NH/OH ratio R as a function of the filling of the pores. At high filling ratios, separate NMR signals were observed for MPz in the internal, external, and outside spaces, which allowed us to characterize the guest capacity of the internal pores. The results are then discussed and modeled in terms of a cylindrical pore structure corrected for the roughness of the inner surfaces.

EXPERIMENTAL SECTION

^{1}H NMR spectra were measured under MAS conditions using a Varian Infinity Plus instrument, equipped with an Oxford wide-bore (9 cm) superconducting magnet of 7.1 T (300.13 MHz ^{1}H frequency) and a Varian 6 mm Chemagnetics pencil probe. Dry air was used for rotor bearing, driving, and heating via three separate gas lines. The sample temperatures were established using a Chemagnetics CMX temperature controller. The spinning rates were adjusted to 5 kHz. The chemical shifts were referenced to an external sample of solid sodium-3-trimethylsilyl-propionate (TSP). All spectra were measured using 90° pulses of about 4 μs duration with pulse delays of 5 s, sufficient enough to achieve full ^{1}H longitudinal relaxation, as the longitudinal relaxation times were shorter than 1 s.

Liquid 4-methyl-1*H*-pyrazole 99% was purchased from Sigma-Aldrich and used without further purification.

The MCM-41 (2.9 nm pore diameter) and SBA-15 (8.9 nm pore diameter) materials were taken from batches studied previously,[39] synthesized by Findenegg et al.[35] Since the materials are highly hygroscopic, they were dried at 10^{-6} mbar and 100 °C for 24 h before use. Contact with air was avoided as far as possible during the sample preparation and subsequent measurements. The solid-state ^{1}H MAS NMR spectra were similar to those described before.[39]

The samples were prepared at room temperature as follows. An empty 6 mm rotor was weighed, including its homebuilt cap. The desired amount of MCM-41 or SBA-15 was loaded into the rotor, dried under vacuum, closed with the cap, and weighed. After taking an initial ^{1}H MAS NMR spectrum, the rotor cap was shortly removed, and using a microsyringe, a known volume of MPz was added. Then, the sample was closed and weighed again. After that, it was stored overnight at room temperature in an evacuated closed glass vessel to ensure that the diffusion through the matrix was complete. The following day, the ^{1}H MAS NMR spectrum was taken at 398 K. This cycle was repeated several times, during which successive amounts of MPz were added.

Measurements of neat MPz were performed using special homebuilt Teflon inserts for 6 mm MAS rotors. A list of all samples is included in Tables S1 and S2 of the Supporting Information.

RESULTS

^{1}H MAS NMR Spectra of 4-Methyl-1*H*-pyrazole inside MCM-41 and SBA-15. We prepared various samples of MCM-41 and SBA-15 containing different amounts of MPz. The compositions of the samples were characterized by the overall MPz/silica mass ratio

$$W = \frac{m_{\mathrm{MPz}}}{m_{\mathrm{silica}}} \tag{1}$$

The weight ratios of all samples are listed in Tables S1 and S2 of the Supporting Information.

The ^{1}H MAS one-pulse NMR spectra of a sample of MPz in MCM-41 with W = 0.379 at 298 and 398 K are depicted in Figure 2. The aromatic CH signal appears at 7 ppm and the methyl signal at 1.7 ppm. These signals do not change their position with temperature. Their line width decreases only to a small extent when heating the sample. This indicates a fast rotational diffusion of MPz in the sample. By contrast, a broader signal is observed at 298 K around 10 ppm, which

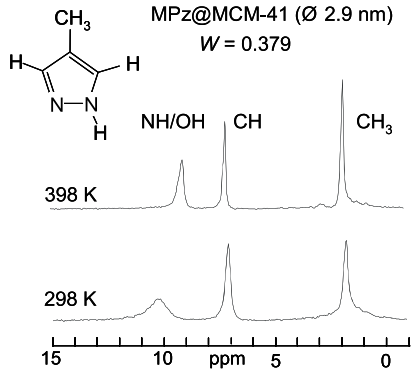

Figure 2. ^{1}H single 90° pulse NMR spectra of 4-methyl-1*H*-pyrazole (MPz) embedded MCM-41 (2.9 nm pore diameter, MPz/silica ratio 0.379, 5 kHz spinning speed) at 298 and 398 K.

https://dx.doi.org/10.1021/acs.jpcc.0c04889
J. Phys. Chem. C 2020, 124, 22082−22095

shifts to about 9 ppm when the temperature is increased to 398 K. We assign this signal to the mobile protons of the sample, i.e., to the NH protons of MPz and to the surface SiOH protons, which are subjected to fast proton exchange and hence signal coalescence. At room temperature, the coalesced NH/OH signal still contains some exchange broadening, which disappears only at high temperatures when the proton exchange is ultrafast. The observed shift to a high field arises from the breaking of hydrogen bonds.

To minimize the effects of exchange broadening, we therefore choose 398 K as the temperature where all subsequent experiments were carried out. This temperature is still far from the boiling point of MPz at 477 K.[10] All spectra measured are included in Figures S1 and S2 of the Supporting Information. Here, in Figure 3, for the sake of clarity, only some typical spectra measured are depicted.

For comparison, Figure 3a shows the spectrum of neat liquid MPz at 398 K. The NH signal of neat liquid MPz at 398 K now appears at 12 ppm, whereas a value of 13 ppm is observed at 298 K (not shown). Again, the difference arises from the partial dissociation of hydrogen-bonded MPz complexes when the temperature is increased. We expect that the cyclic trimers are formed as in the crystalline state dominantly.[16]

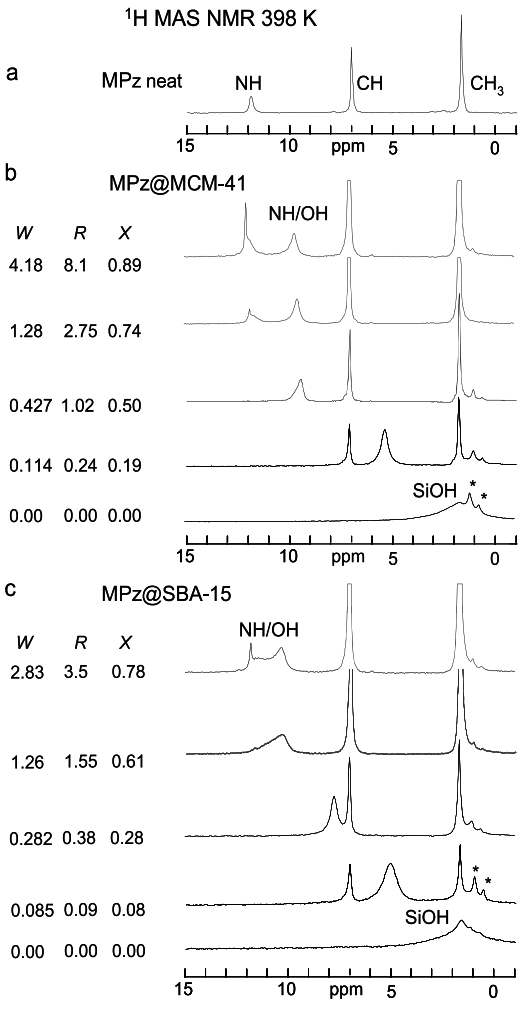

Figure 3. Some typical ^{1}H single 90° pulse NMR spectra at 398 K and 7 T of 4-methyl-1*H*-pyrazole (MPz) in different environments. Additional spectra are depicted in Figure S1. (a) Neat bulk liquid (3 kHz spinning speed). (b) MPz loaded into MCM-41 (2.9 nm pore diameter, 5 kHz spinning speed) and (c) loaded into SBA-15 (8.9 nm pore diameter, 5 kHz spinning speed). The vertical expansion of the spectra was adjusted arbitrarily to optimize the representation of the NH/OH signals. For the signal assignment, see the text.

Neat guest-free MCM-41 and SBA-15 samples give rise to well-known signals for non-hydrogen-bonded surface SiOH groups around 1.75 ppm (Figure 3).[39] The spectra measured at 398 K exhibit some line broadening, whose origin was not further elucidated in the present study. In some samples, we observed two weak sharp signals around 1 ppm characterized in Figure 3 by asterisks; we found out that they stem from small amounts of grease from the high-vacuum glass apparatus used for sample preparation.

As illustrated in Figures 3 and S1, the addition of MPz to silica materials leads to low-field shifts of the coalesced NH/OH signals. These shifts arise from two different phenomena, (i) the increase of the mole fraction of MPz, which resonates at a low field and (ii) the formation of hydrogen bonds between the SiOH groups and the aromatic nitrogens of MPz. The latter is similar to the case of pyridine added to mesoporous silica, where surface −SiOH···pyridine hydrogen bonding leads to a low-field shift from 1.75 to 10 ppm.[39]

For samples with an excess of MPz, an unexpected effect is observed: the coalesced NH/OH signals cease to shift further to a low field in the presence of additional MPz, but new coalesced NH/OH signals appear close to the NH signal of neat liquid MPz. These different coalesced NH/OH signals stem from different local environments, which we assign to internal, external, and outside spaces labeled as l = int, ext, and out, respectively. These environments exhibit different NH/SiOH ratios $R(l)$.

Data Analysis. In the first step, we determined the overall molar ratio of the NH groups of MPz vs the number of surface SiOH groups of silica

$$R = \frac{N_{NH}}{N_{OH}} \tag{2}$$

As R becomes very large for samples characterized by a large excess of the MPz guest, we also used the overall mole fraction of the NH groups given by

$$X \equiv X_{NH} = (1 - X_{OH}) = \frac{N_{NH}}{N_{NH} + N_{OH}} = \frac{R}{1 + R},$$
$$R = \frac{X_{NH}}{1 - X_{NH}} \tag{3}$$

where X_{OH} represents the fraction of surface SiOH groups.

The values of R were obtained by signal integration, taking into account that the number of the aromatic CH groups is twice that of the NH groups. R is given by

$$R = \frac{N_{NH}}{N_{OH}} = \frac{N_{CH}}{2N_{OH}} = \frac{N_{CH}}{2\left(N_{OH} + N_{NH} - \frac{N_{CH}}{2}\right)}$$
$$= \frac{I_{CH}}{2I_{NH/OH} - I_{CH}} \tag{4}$$

Here, I_{CH} stands for the intensity of the aromatic proton signals and $I_{NH/OH}$ for the intensity of the coalesced NH/OH signals. All three quantities characterizing the sample composition, i.e., W, R, and X, are included in Figure 3.

https://dx.doi.org/10.1021/acs.jpcc.0c04889
J. Phys. Chem. C 2020, 124, 22082−22095

In the next step, our aim was to know that the guest molecules MPz are distributed between the different spaces as a function of the overall filling fraction.

The ratio of NH vs OH groups in space l is given by

$$R^l = \frac{N_{NH}^l}{N_{OH}^l}, \quad l = \text{int}, \text{ ext}, \text{ out} \tag{5}$$

and the corresponding fraction of NH groups by

$$x^l = \frac{N_{NH}^l}{N_{NH}^l + N_{OH}^l} \tag{6}$$

The fraction of mobile NH/OH groups in space l with respect to the total number of mobile NH/OH groups is given by

$$p^l = \frac{N_{NH}{}^l + N_{OH}{}^l}{N_{NH} + N_{OH}} \tag{7}$$

The fraction of MPz molecules in space l with respect to the total number of MPz molecules can be calculated from the values of $x(l)$, $p(l)$, and X according to

$$\frac{N_{NH}{}^l}{N_{NH}} = \left(\frac{N_{NH}{}^l}{N_{NH}{}^l + N_{OH}{}^l}\right)\left(\frac{N_{NH}{}^l + N_{OH}{}^l}{N_{NH} + N_{OH}}\right)\left(\frac{N_{NH} + N_{OH}}{N_{NH}}\right) = \frac{x^l p^l}{X} = x^l p^l\left(1 + \frac{1}{R}\right) \tag{8}$$

once x^l, p^l, and X or R have been obtained from the spectra. By multiplication with the total mass of MPz, we then obtain the mass of MPz, which enters a given space l

$$m^l = \frac{N_{NH}^l}{N_{NH}} m_{MPz} \tag{9}$$

To compare the different samples, it is convenient to divide by the total mass of silica, which leads to the relative mass ratio W^l of the guest in the different spaces

$$W^l = \frac{m_{MPz}^l}{m_{silica}} = \frac{N_{NH}^l}{N_{NH}}\frac{m_{MPz}}{m_{silica}} = \frac{N_{NH}^l}{N_{NH}} W = \frac{x^l}{X} p^l W \tag{10}$$

We will use eq 10 to interpret the filling results described in the following. To obtain the values of p^l, we performed the lineshape analyses of the coalesced NH/OH signals depicted in Figure 4. We assumed a slow guest exchange between the different spaces. The values obtained are included in Table 2. To determine the values of the NH fractions x^l in the different spaces needed in using eq 10, we proceeded as follows.

First, we plotted in Figure 5 the chemical shifts $\delta_{NH/OH}$ of the averaged NH/OH signals as a function of the overall NH fraction $X = R/(1 + R)$. The filled data points in Figure 5 (see Tables S1 and S2) were taken from the samples containing only a single coalesced NH/OH signal for which $X = x^{int}$. We included the data point of neat MPz at $X = 1$. Then, we searched for an empirical function $\delta_{NH/OH} = f(X)$ to represent the filled data points. We found that eq 11 visualized in Figure 5 as a solid curve represented all data points very well, both for MCM-41 and SBA-15. In the next step, we took the experimental $\delta_{NH/OH}$ chemical shifts obtained by lineshape analysis (Figure 4) and placed them as open symbols on the solid line by adapting the corresponding x^l values for each sample and space l.

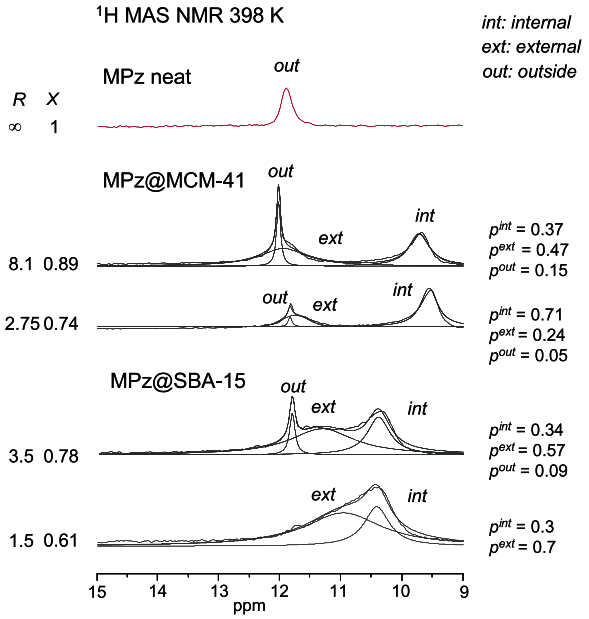

Figure 4. Lineshape analyses of the ^{1}H MAS NMR spectra of Figure 3. The vertical expansion of the spectra was adjusted arbitrarily to optimize the representation of the NH/OH signals. For further explanation, see the text.

$$\delta_{NH/OH} = 1.75 + 21.8\left[1 - \frac{1}{3.1X}[\sqrt{6.1X + 1} - 1]\right] \tag{11}$$

Host–Guest Filling Diagrams. In Figure 6, the values of W^{int}, W^{ext}, and W^{out} of MPz are plotted as a function of the total weight ratio $W = W^{int} + W^{ext} + W^{out}$. The dotted lines were not calculated but represented as a guide for the eye.

In the case of MCM-41, until a weight ratio W of about 1, only the internal pores are filled successively as the total amount of MPz is increased. Above this threshold, in addition to the internal pores, the space between the pores is filled, but the space outside is still empty. Above a mass ratio of 2, more MPz is observed in the external space, but the internal space continues to be filled until the highest value of the filling ratio W is obtained. At a mass ratio of 4, a substantial amount of MPz enters the outside space, but most of MPz is located in the external volume.

In the case of SBA-15, initially, only the internal pores are successively filled, but then the increase is reduced at the expense of the external space. Already at a mass ratio of 1, most MPz molecules are located in the latter. The outside space is filled in a similar way as in the case of MCM-41.

In Figure 7, we have plotted the individual NH fractions x^l as a function of the total NH fraction X of the mobile NH and OH protons. X represents another measure for the filling fraction (see eq 3). The individual NH mole fractions of MPz in the external spaces of MCM-41 and of SBA-15 are about 0.8 or higher, even when the internal spaces are far from being filled with MPz molecules, as a comparison of the data points in Figure 7 with those of Figure 5 shows. This is not compatible with the formation of monolayers exhibiting small NH/OH ratios but with the formation of small liquid clusters exhibiting much more guest–guest interactions than host–guest interactions. This point will be discussed later in more detail.

However, the line widths (see Figure 4) are large, suggesting a distribution of microspaces with somewhat different S/V

https://dx.doi.org/10.1021/acs.jpcc.0c04889
J. Phys. Chem. C 2020, 124, 22082–22095

Table 2. Composition of Samples of 4-Methyl-1*H*-pyrazole (MPz) in Mesoporous Silica at 398 K Determined by the Integration of the Signals of the ^{1}H MAS NMR Spectra in Figures 3 and 4[a]

W	R	X	component l	NH/OH signal δ^l (ppm)	p^l	R^l	x^l
4-Methyl-1*H*-pyrazole Neat Liquid							
∞	∞	0	0	11.9	1.0	∞	1.0
4-Methyl-1*H*-pyrazole/MCM-41 Pore Diameter 2.9 nm							
0	0	0	int	1.75	1.0	0	0
0.114	0.24	0.19	int	5.4	1.0	0.24	0.19
0.427	1.02	0.51	int	9.5	1.0	1.02	0.50
1.28	2.75	0.73	int	9.6	0.71	1.17	0.54
			ext	11.7	0.24	19	0.95
			out	11.8	0.05	∞	1
4.18	8.13	0.89	int	9.7	0.37	1.33	0.57
			ext	11.9	0.47	30	0.97
			out	12.0	0.15	∞	1.00
4-Methyl-1*H*-pyrazole/SBA-15 Pore Diameter 8.9 nm							
0	0	0	int	1.75	1.0	0	0
0.085	0.09	0.083	int	5.1	1.0	0.09	0.083
0.282	0.38	0.275	int	7.9	1.0	0.38	0.275
1.26	1.55	0.61	int	10.4	0.3	1.86	0.65
			ext	11.0	0.7	3.5	0.78
2.83	3.5	0.78	int	10.4	0.34	1.94	0.66
			ext	≈11.3	0.57	≈6	≈0.86
			out	11.8	0.09	∞	1

[a] W is the MPz/silica sample mass ratio. R is the NH/OH ratio determined by signal integration using eq 4. X is the corresponding NH mole fraction of the ensemble of NH and OH groups. δ^l: the chemical shift of NH/OH signal l in Figure 3. p^l: the fraction of signal l in Figure 4 with respect to the total NH/OH signal intensity as determined by lineshape analysis. R^l: the NH/OH ratio of space l. x^l: the NH mole fraction of mobile protons in space l determined by accommodating the experimental chemical shifts δ^l to the solid line in Figure 5.

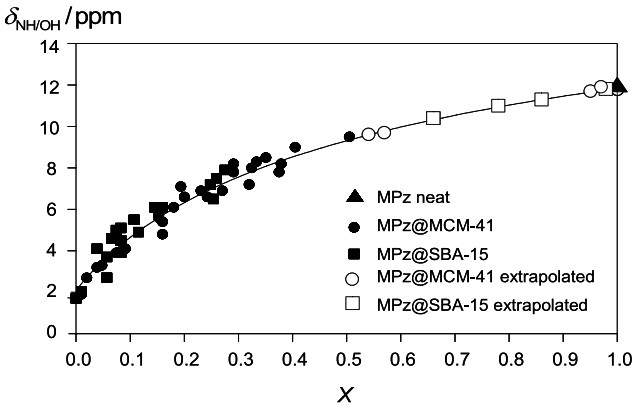

Figure 5. Chemical shifts δ of the averaged NH/OH groups of MPz inside mesoporous silica of the MCM-41 and SBA-15 types as a function of the MPz/SiOH mole fraction X. The solid line was calculated using the empirical relation of eq 11. Filled symbols stem from spectra exhibiting only a single averaged NH/OH signal. Open symbols refer to the spectra exhibiting more than one averaged NH/OH signal. Their chemical shifts were placed on the solid line from which the individual MPz vs SiOH mole fractions x^l, l = int, ext, and out were obtained.

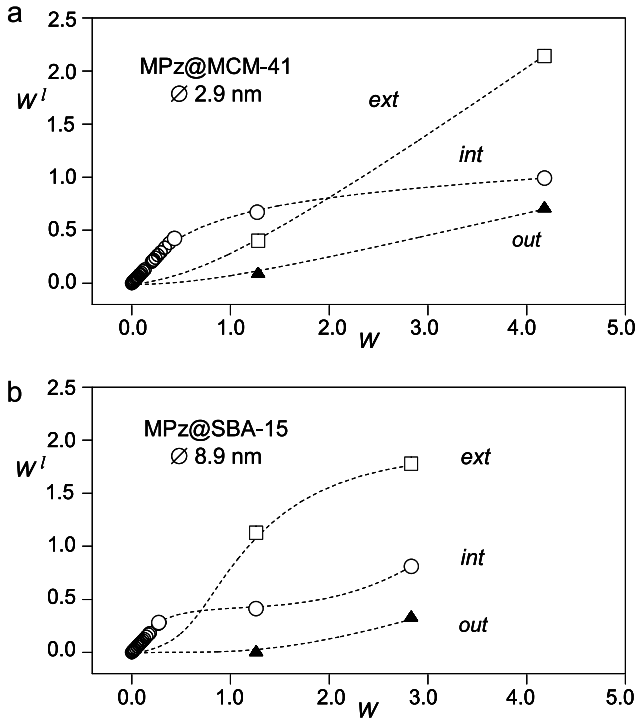

Figure 6. Uptake of MPz as the guest in the different spaces l = int, ext, and out of MCM-41 and SBA-15 samples. The abscissa represents the total weight W of MPz incorporated per 1 g of silica. The ordinate represents the partial weight W^l (eq 10) loaded into space l. The solid lines are guidelines for the eye. For further explanation, see the text.

ratios. That is not surprising, as the silica crystallites are not ordered with respect to each other. Naturally, the mole fraction of MPz in the outside space is unity.

The results obtained for the internal spaces are also astonishing for both MCM-41 and SBA-15. In the early stages of the filling, the NH fraction inside the internal pores increases linearly with the total NH fraction as expected for the formation of submonolayers, which then increase to monolayers. However, above an NH fraction of about 0.5−0.6, the increase of the NH fraction of the internal pores stops, although they continue to be filled as is illustrated in Figure 6a. The final NH fractions in the internal pores are about 0.6. This means that in the internal pores, the NH groups of MPz

https://dx.doi.org/10.1021/acs.jpcc.0c04889
J. Phys. Chem. C 2020, 124, 22082−22095

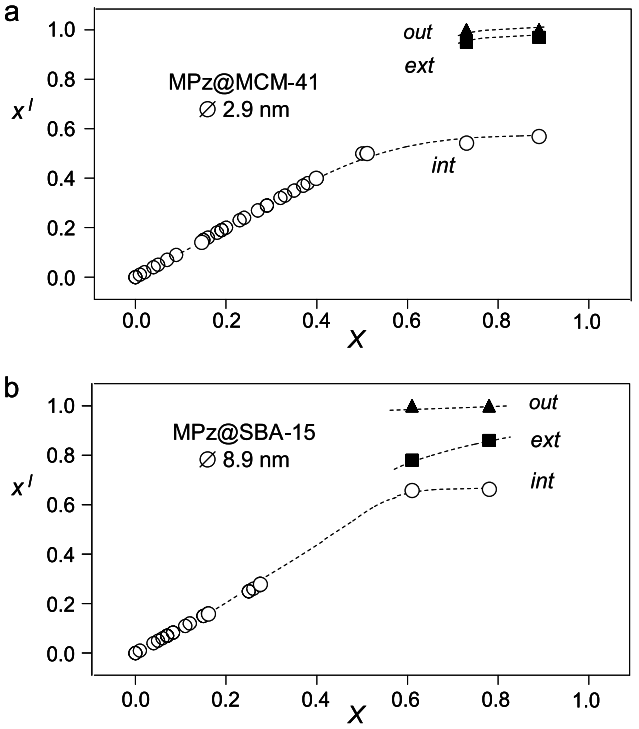

Figure 7. Individual MPz vs SiOH mole fractions x^I of MPz/silica samples as a function of the total MPz mole fraction X. The solid lines are guidelines for the eye. For further explanation, see the text.

represent 60% of the exchangeable protons and the SiOH groups 40%. For MCM-41, the value is slightly less than 60% and for SBA-15 slightly larger.

All values determined from the ^{1}H MAS spectra are included in Table 2. The implications of these findings are discussed in the next section.

DISCUSSION

By measuring the ^{1}H MAS NMR spectra of 4-methyl-1*H*-pyrazole (MPz) in mesoporous silica of the MCM-41 and SBA-15 type at 398 K as a function of the pyrazole/silica ratio in the regime of fast host−guest proton exchange, we have obtained a number of parameters that provide information about the filling of the silica pores and the state of MPz inside the pores. The purpose of this discussion is to describe this information in detail.

Our first aim is to discuss the results obtained for the silica materials, which are fully loaded with the MPz guest. We will derive the number of molecules in the different spaces and the surface/volume, surface/surface, and volume/volume ratios for the internal pores and external spaces. A surface-roughness-corrected cylindrical pore (SRCCP) model will be developed, which enables the comparison with other analytical methods such as the BET technique. In the next step, we will discuss the filling processes of the different cavities and their competition for receiving the MPz guest molecules. Finally, we will discuss the role of host−guest and guest−guest hydrogen bond formation.

Sample Structures. *Surface-Roughness-Corrected Cylindrical Pore Model (SRCCP Model) to Predict the Number of MPz Guest Molecules in the Internal Pores of MCM-41 and SBA-15.* To elucidate how many MPz molecules can enter a given space, we first need to estimate the volume of a single MPz guest molecule at 398 K. This molecular volume is given by

$$\upsilon_{MPz} = M_{MPz}/\rho N_A \quad (12)$$

M_{MPz} is the molar mass, ρ is the density of liquid MPz at 398 K, and N_A is Avogadro's number. As indicated in Table 3, the density of MPz has been reported for the solid at 100 K by Goddard et al.,[16] whereas Auwers et al.[10] measured two values of ρ around room temperature. As we could not find any other experimental density data of MPz in the literature, we plotted the three values as a function of temperature, which gave a perfectly linear dependence (see Figure S3) with a slope typical for a number of organic solvents,[61] and finally adopted the extrapolated value of 0.92 g cm^{-3} at 398 K. The latter gave a molecular volume of υ_{MPz} = 0.148 nm^3 for a single MPz molecule.

Table 3. Molecular Volume of Liquid 4-Methyl-1*H*-pyrazole (MPz)

molar mass		M	82.106 g mol^{-1}
density solid 100 K	ref 16	ρ	1.19 g cm^{-3}
density liquid 289.9 K	ref 10	ρ	1.0183 g cm^{-3}
density liquid 293.2 K	ref 10	ρ	1.015 g cm^{-3}
density liquid 398 K	extrapolated	ρ	0.92 g cm^{-3}
molar volume 398 K		M/ρ	89.25 × 10^{21} nm^3 mol^{-1}
molecular volume	eq 12	υ_{MPz}	0.148 nm^3

In Table 1, we had already assembled some main properties of the two silica samples studied. From the BET specific surface areas and pore volumes, we calculated the BET surface/volume ratios S^{BET}/V^{BET} of 1.5 nm^{-1} for the MCM-41 sample and 0.7 nm^{-1} for the SBA-15 sample. For comparison, we calculated the corresponding values of a cylindrical tube with length l and diameter d (Figure 8a).

$$S^{cyl}/V^{cyl} = \frac{\pi l d}{\pi l (d/2)^2} = 4/d \quad (13)$$

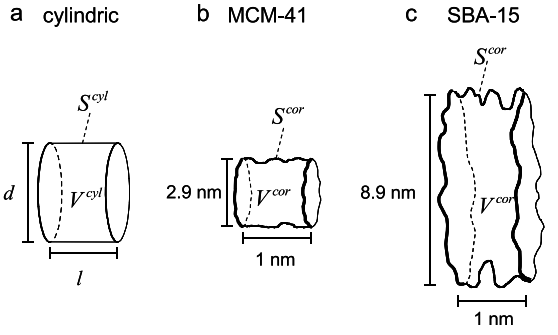

Figure 8. Models of internal pore segments of mesoporous silica. (a) Cylindric pore segment. (b, c) Surface-roughness-corrected cylindrical pore (SRCCP) segments schematically representing the situation of the MCM-41 and SBA-15 samples.

Equation 13 gives a similar value, i.e., 1.4 nm^{-1} for the MCM-41 sample but a somewhat smaller value of 0.45 nm^{-1} for the SBA-15 sample. We assign this difference to the different roughness of the inner pore surfaces as stated before,[39] which is moderate in the case of MCM-41 but large for SBA-15 as illustrated schematically in Figure 8.

https://dx.doi.org/10.1021/acs.jpcc.0c04889
J. Phys. Chem. C 2020, 124, 22082−22095

We found that the cylindrical model can be modified in a simple way to take the surface roughness into account. We assume that the pore volume is not much affected by the surface roughness, i.e.

$$V^{cor} = V^{BET} \cong V^{cyl} \quad (14)$$

By contrast, the real surface is larger than that calculated for a cylindrical tube. Let F be a correction factor, which transforms the cylindrical surface into the correct one

$$S^{cor} = FS^{cyl} \quad (15)$$

By a combination of eqs 14 and 15, it follows that F can be evaluated from the experimental BET surface/volume ratio

$$\frac{S^{cor}}{V^{cor}} = F\frac{S^{cyl}}{V^{cyl}} \cong \frac{S^{BET}}{V^{BET}} \quad (16)$$

Thus, using the experimental surface areas and specific volumes, we are able to calculate the surface/volume ratios for any pore segment of length l = 1 nm and diameter d using the SRCCP model, as illustrated in Table 4. Naturally, the corrected ratios are the same as those obtained by BET. Using eq 15 and the experimental pore diameters, we obtain for such a pore segment a surface area of 9.9 and 44 nm^2 for the MCM-41 and SBA-15 samples, respectively.

Table 4. Properties of Internal Pore Segments of Length l = 1 nm and Diameter d Calculated Using the SRCCP Model for the MCM-41 and SBA-15 Materials Studied

	variable/equation	MCM-41	SBA-15
volume of a cylindrical pore segment (nm^3)	V^{cyl}	6.61	62.2
surface area of cylindrical pore segment (nm^2)	S^{cyl}	9.11	28.0
surface/volume ratio of a cylindrical pore segment (nm^{-1})	S^{cyl}/V^{cyl} eq 13	1.38	0.45
surface correction factor, F	$F = \frac{S^{cor}}{V^{cor}}/\frac{S^{cyl}}{V^{cyl}}$ eq 16	1.083	1.57
corrected surface/volume ratio of pore segment (nm^{-1})	$\frac{S^{cor}}{V^{cor}} = \frac{S^{BET}}{V^{BET}}$	1.495	0.707
corrected volume of pore segment (nm^3)	V^{cor} eq 14	6.61	62.2
corrected surface of pore segment (nm^2)	S^{cor} eq 15	9.87	44
number of surface silanol groups in pore segment	$N_{OH}^{cor} = n_{SiOH}S^{cor}$	29.6	163
number MPz in full pore segment	$N_{MPz}^{cor} = V^{cor}/v_{MPz}$ eq 17	45	420
number MPz/number OH ratio in full pore segment	$R^{cor} = N_{MPz}^{cor}/N_{OH}^{cor}$	1.52	2.58

The numbers n_{OH} of SiOH groups per surface area can be calculated from the values obtained previously by NMR by some of us.[39] In that study, n_{OH} = 3.0 SiOH groups per nm^2 were found for MCM-41 and 3.7 per nm^2 for SBA-15. These values lead here to 29.6 SiOH groups for the MCM-41 pore segment and 163 SiOH groups for the SBA-15 pore segment. For comparison, crystalline silica surface values of about 4.5 per nm^2 were reported.[39,62]

The maximum number of MPz in a filled pore segment is given by

$$N_{MPz} = \frac{V^{cor}}{v_{MPz}} = \frac{\pi l d^2 \rho N_A}{4M_{MPz}} \quad (17)$$

where v_{MPz} is the molecular volume of MPz, ρ is the density of MPz at 398 K, and N_A is Avogadro's number. As illustrated in Table 4, for the filled pore segment, we then obtain N_{MPz} = 45 molecules of MPz in MCM-41 and 420 in SBA-15, corresponding to the molar NH/OH ratios $R^{cor} = N_{MPz}^{cor}/N_{OH}^{cor}$ of about 1.5 and 2.6 or to the NH mole fractions $X^{cor} \equiv X_{NH}^{cor} = R^{cor}/(1 + R^{cor})$ of 0.6 and 0.7.

Comparison of the SRCCP Model Results with Those Obtained by NMR. The SRCCP model, which is based on the BET technique, can only describe the regular internal pores of mesoporous silica but not the irregular external spaces between crystallites because of the orientational disorder. By contrast, using the NMR-detected host−guest proton exchange, we obtained the data for both types of cavities that are assembled in Table 5. In the following, we assume that both the internal pores as well as the external spaces are entirely filled in the case of the samples containing the largest amounts of MPz. This is justified as, in these cases, the outside space (Figure 1) contained substantial amounts of neat liquid MPz (Figures 3 and 4).

Table 5. Properties of the MCM-41 and SBA-15 Materials Containing 4-Methyl-1*H*-pyrazole (MPz) Obtained by NMR (This Work)

		MCM-41	SBA-15
experimental NH/OH ratio[a]	$R^{int} = N_{MPz}^{int}/N_{OH}^{int}$	1.33	1.94
number of MPz molecules in filled internal pore segment	$N_{MPz}^{int} = R^{int}N_{OH}^{cor}$	39.4	316
S/V ratio of internal pores (nm^{-1})	$\frac{S^{int}}{V^{int}} = \frac{1}{n_{SiOH}R^{int}v_{MPz}}$	1.69	0.94
experimental NH/OH ratio[a]	$R^{ext} = N_{MPz}^{ext}/N_{OH}^{ext}$	≈30	≈6
S/V ratio of external space (nm^{-1})	$\frac{S^{ext}}{V^{ext}} = \frac{1}{n_{OH}R^{ext}v_{MPz}}$	≈0.075	≈0.30
external/internal volume ratio[a]	$\frac{V^{ext}}{V^{int}} \cong \frac{p^{ext}}{p^{int}}$	1.27	1.68
external/internal surface ratio	$\frac{S^{ext}}{S^{int}} = \frac{V^{ext}}{V^{int}}\frac{S^{ext}}{V^{ext}}\frac{V^{int}}{S^{int}}$	0.053	0.54
surface correction factor, F	$F = \frac{S^{int}}{V^{int}}/\frac{S^{cyl}}{V^{cyl}}$	1.225	2.09

[a]Values taken from Table 2.

Among other data, we obtained the experimental molar NH/OH ratios $R^{int} = N_{MPz}^{int}/N_{OH}^{int}$ of 1.33 for the internal pores of MCM-41 and of 1.94 for SBA-15 or to the NH mole fractions $X^{cor} \equiv X_{NH}^{int} = R^{int}/(1 + R^{int})$ of 0.57 and 0.66. These values are in good agreement with those obtained using the BET data of the SRCCP model (Table 4); the mole fractions are identical to the experimental data obtained for the largest total MPz mole fraction X on the right side of Figure 6. If we assume that the number of surface SiOH groups is well described by the value of N_{OH}^{cor} in Table 4, we obtain by NMR 39 MPz molecules for a filled pore segment of MCM-41 and 316 for SBA-15. These numbers are slightly smaller than the ones estimated using the SRCCP model.

For a direct comparison, we calculated the surface/volume ratios entirely from the NMR data, assuming that the pores are full in the samples containing the highest amounts of MPz. In addition, we assume that the number n_{OH} of SiOH groups per surface area is the same in the internal pores and the external void spaces. Then, the surface obtained from NMR data is given by

https://dx.doi.org/10.1021/acs.jpcc.0c04889
J. Phys. Chem. C 2020, 124, 22082−22095

$$S^l = \frac{N^l_{OH}}{n_{OH}} = \frac{N^l_{MPZ}}{n_{OH}R^l}, \quad l = \text{int}, \text{ ext} \tag{18}$$

for both the internal and the external spaces, and the volumes by

$$V^l = N^l_{MPz}\upsilon_{MPz}, \quad l = \text{int}, \text{ ext} \tag{19}$$

It follows that

$$\frac{S^l}{V^l} = \frac{1}{n_{OH}R^l\upsilon_{MPz}}, \quad l = \text{int}, \text{ ext} \tag{20}$$

Table 5 shows that the internal surface/volume ratios obtained by NMR, i.e., 1.69 and 0.94 nm^{-1} for both materials compare well with those of the SRCCP model, i.e., with the BET values of 1.5 and 0.7 nm^{-1} (Table 4). In view of the complex structure of the materials and the number of possible systematic errors, the agreement of the BET and NMR methods is very satisfactory.

For the internal pores of MCM-41, the S/V ratio is more than 20 times larger than for the external space. In addition, the experimental NH/OH ratio of the external space of MCM-41 is much larger than that of the internal pores. This means that the external surface is much smaller than the internal one, and it is justified to neglect the external surface of MCM-41 when interpreting surface data obtained by the BET method.

However, this is not true for SBA-15, where the S/V ratio of the internal pores is only 3 times larger than of the external spaces. This indicates that the "advantage" of ordered pores in SBA-15 is much less pronounced.

Finally, we were able to evaluate the external and internal surface/surface and volume/volume ratios by NMR. For this, we assume that the relative amounts $p(l)$ of MPz in the external and internal spaces obtained by lineshape analysis (Figure 4 and Table 2) can be interpreted in terms of the volume ratio

$$\frac{V^{ext}}{V^{int}} \cong \frac{p^{ext}}{p^{int}} \tag{21}$$

By combination with the surface/volume ratios of Table 5, we then obtain also the external/internal surface ratios

$$\frac{S^{ext}}{S^{int}} = \frac{V^{ext}}{V^{int}}\frac{S^{ext}}{V^{ext}}\frac{V^{int}}{S^{int}} \tag{22}$$

The results are included in Table 5. We are surprised that the external volumes are between 30 and 70% larger than the internal volumes. These results might depend on magic-angle spinning (MAS, see Figure 1), which could compress the external volumes.

On the other hand, the external surface of MCM-41 represents only 5% of the internal surface, whereas the external surface of SBA-15 represents more than 30% of the internal surface.

In principle, it is possible using NMR to measure the volume ratios of different samples, e.g., of MCM-41 vs SBA-15 for the internal and external spaces. However, this requires the parallel measurement of standardized samples, a procedure that was beyond the scope of this study. Moreover, for comparison, the densities of the pure silica samples should also be known to evaluate the ratio of the free volumes to the total sample volumes.

Host–Guest Filling Behavior. Figures 6 and 7 indicate that guest molecules enter first the internal space, then the external, and the outside space. However, the external space starts to be filled before the internal space is full, and the situation is similar for the outside and external spaces.

To understand this host–guest filling behavior of the silica samples studied, we need to recall some results of Table 5. For MCM-41, the internal surface is 20 times larger than the external surface, whereas it is only 3 times larger for SBA-15. By contrast, the internal and external volumes are similar. In this section, we discuss whether the above-mentioned structural features are able to explain the observed host–guest filling behavior depicted in Figures 6 and 7.

Two questions are addressed, (i) why does MPz populate preferentially the internal pores at low filling fractions but the external spaces at large fractions? And (ii) why is the final MPz/SiOH fraction for the internal pores already achieved even if the pores are not yet filled?

We will try to answer these questions in a qualitative way, as depicted in Figure 9, for a well-ordered porous silica material.

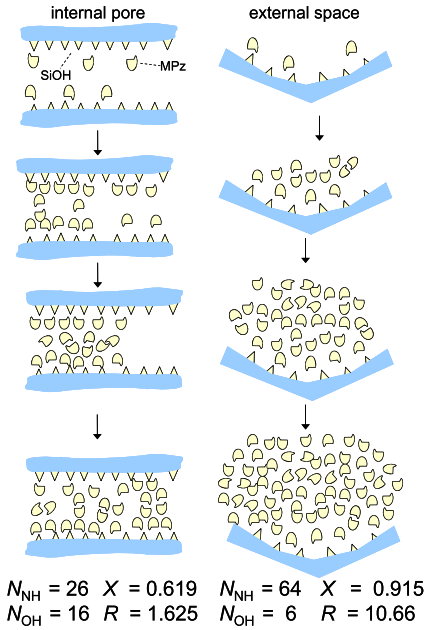

Figure 9. Simplified filling scenario of MPz guests in mesoporous silica. The left column refers to internal pores characterized by very large internal surface/volume ratios. Different stages are considered, e.g., submonolayer formation, monolayer formation with a tendency to form liquid clusters, cluster formation exhibiting the final NH/OH ratio, and filled pore. The right column refers to external spaces, exhibiting small surface/volume ratios. In the beginning, MPz molecules enter mainly the internal pores but eventually they populate the larger volumes of the external space dominantly. For further explanation, see the text.

The surface SiOH groups are symbolized by yellow triangles and the MPz guest molecules by yellow forms, where the polar NH groups are also represented by triangles and the nonpolar aromatic side by the rounded parts. Figure 9 shows on the left side a scenario for internal regular pores and on the right side for irregular external spaces or irregular internal pores. To symbolize the small surface/volume ratio, only a small surface is shown in contact with a much larger volume around.

At small filling fractions, submonolayers are formed on both internal and external surfaces where the guests attach to the

https://dx.doi.org/10.1021/acs.jpcc.0c04889
J. Phys. Chem. C 2020, 124, 22082–22095

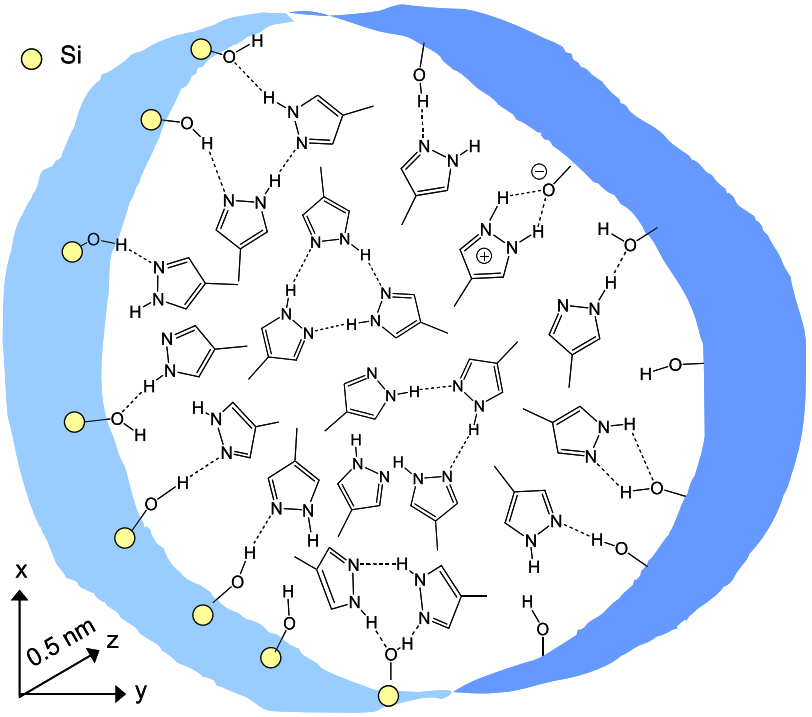

Figure 10. Molecular scenario of MPz molecules in a half pore segment of MCM-41 of 0.5 nm length and 3 nm diameter. According to the NMR data analyses of Table 5, 20 MPz molecules were placed inside the pore and 15 SiOH groups (Table 4) on the silica surface. Thirteen MPz molecules were considered to form surface-hydrogen bonds. Seven MPz molecules are located in the core, either free or forming various types of hydrogen-bonded complexes, for example, a cyclic dimer observed in neat MPz crystals.[16] Surface 1:1 MPz/SiOH complexes exhibiting O−H···N hydrogen bonds are expected to be stronger than O···H−N hydrogen bonds.[66] The mechanism of host−guest proton exchange is unknown. It probably takes place in surface guest−host complexes via multiple proton transfers, possibly involving H-bond rearrangements and zwitterionic intermediates or transition states.[14] For further explanation, see the text.

surface SiOH groups via hydrogen bonding. This explains the finding in Figure 6 that at low filling fractions, MPz molecules are located only on the surface.

The situation changes when the formation of a monolayer is approached. Then, the number of SiOH groups is similar to the number of MPz molecules. The absence of vacancies leads to a decrease of the binding entropy. A second and a third layer are rapidly formed where hydrogen bonds to the first layer are unlikely. At this stage, there is no advantage for guests to enter the internal pores anymore. The critical importance of specific guest−surface interactions for the uptake and localization of the guest into pores was demonstrated in the past for different guests.[63−65] Thus, it is understandable that at this stage, more guest molecules enter the external space, as revealed in Figure 6. Then, in both spaces, the internal and external ones, small droplets may be formed, whose size is limited in the pores by the close distance between the walls, in contrast to the external spaces. As a result, the final NH/OH ratio in certain pore segments may be achieved before the whole pore is filled because some segments will be locally filled, whereas others remain more or less empty. The individual and the overall NH fraction become similar only in the case of the full pores. Thus, these scenarios can explain both the findings of Figures 6 and 7.

We note that the process of filling the pores of mesoporous silica with water was studied by some of us in the past.[48] For SBA-15, with its larger pore diameter, after an initial coverage of the surface, a radial growth toward the pore axis was proposed. By contrast, for MCM-41, an axial filling of the pores was suggested. This is in agreement with the present observation of the final NH/OH fraction in partially filled pores. On the other hand, in Figure 9, we did not consider yet the more irregular pore surface found for SBA-15 as compared to MCM-41.[39]

Visualization of a Snapshot of MPz Molecules in a Pore Segment of MCM-41 and OH/NH Host/Guest Proton Exchange. Finally, we discuss how MPz molecules might be arranged in a regular pore. As it is difficult to consider SBA-15 with its large surface roughness, we refer here only to MCM-41.

For this system, we have visualized in Figure 10, a pore segment of diameter 3 nm typical for the MCM-41 sample studied filled with MPz. For the sake of clarity, only a segment of length 0.5 nm is depicted, which corresponds approximately to the thickness of an MPz molecule. According to Table 5, such a segment contains then 15 surface SiOH groups, which are arranged about 0.5 nm from each other.[39] In view of the molar NH/OH fraction of 1.33 determined experimentally, we have added 20 MPz molecules into the pore. We let 13 MPz molecules bind to SiOH groups and place 7 molecules inside the core. Figure 10 represents a static scenario, where we have arranged all MPz molecules arbitrarily in the *xy*-plane for the sake of clarity.

The hydrogen-bonded complexes could not be determined in this study, but there are some general aspects that make the choice of complexes depicted in Figure 10 plausible. For the core, we have considered a cyclic trimer in analogy to the crystalline state,[16] a linear trimer and a monomer. Linear dimers could also be formed, and we have depicted a dimer in a hydrogen bond to a surface SiOH group.

https://dx.doi.org/10.1021/acs.jpcc.0c04889
J. Phys. Chem. C 2020, 124, 22082−22095

The different H-bond environments exhibit different chemical shifts in the slow H-bond exchange limit. However, as only a single averaged OH/NH signal is observed for a given pore environment, the exchange between the different hydrogen-bonded environments is fast, in addition to the fast OH/NH proton exchange. This also means a fast molecular rotational and locally translational mobility, indicating that at a given time all MPz molecules should point in different directions.

The hydrogen bond structures of the surface-bound MPz molecules were rationalized as follows. Obvious complexes are 1:1 SiOH−MPz surface complexes, exhibiting either a single O−H···N or an O···H−N hydrogen bond or a cyclic form with both of them. Previously, it has been shown that O−H···N hydrogen bonds are stronger and shorter than O···H−N hydrogen bonds.[66] Moreover, in a cyclic 1:1 complex, both hydrogen bonds are nonlinear, i.e., less stable.

The distance of 0.5 nm between two SiOH groups of MCM-41 seems to be too far for the formation of 2:1 SiOH−MPz complexes, which are, therefore, not included. On the other hand, cyclic 1:2 complexes between the OH groups and two pyrazole molecules have been observed by X-ray crystallography in which a triple proton transfer can take place, and such a complex is depicted in Figure 10.[14]

The presence of some nonhydrogen-bonded NH groups is justified by the observation of a high-field shift of about 1 ppm for neat MPz by increasing the temperature from 298 to 398 K. This indicates the increase of the fraction of nonhydrogen-bonded SiOH and NH groups.

At present, one can only speculate about the mechanism of the host−guest proton exchange between the MPz molecules and the surface SiOH groups. Proton exchange could take place in the 1:1 complexes via a double proton transfer or as a consecutive single proton transfer via a zwitterionic intermediate or a transition state, as illustrated in Figure 10.[67] Also, a triple proton transfer could be realized in the cyclic 1:2 complex in analogy to the related systems.[11−13,66] However, even 2:1 or higher complexes cannot be excluded as intermediates of host−guest proton exchange.

Figure 10 also shows that when the pores are filled, hydrogen bonds are formed between the guest MPz molecules. This phenomenon contributes to the observed low-field shifts of the NH signals of MPz (Figures 3, 5, S1, and S2), in addition to proton exchange between the NH and OH groups. The signals of the SiOH groups will also be shifted downfield upon hydrogen bonding to the MPz molecules. The situation is quite complex, which makes it difficult at present to interpret the shift of the average NH/OH lines to low field upon increasing the guest/host ratio, according to Figure 5.

CONCLUSIONS

The conclusions of the present study can be summarized as follows.

(i) Host−guest proton exchange (HGPE) can be used to obtain information on the filling mechanisms and the structures of porous solids containing surface OH groups using solid-state ^{1}H NMR under MAS conditions. The guest molecules, preferentially heterocyclic compounds, need to exhibit mobile NH groups involved in fast proton exchange with the surface OH groups. The preference of guest molecules for entering the internal, external, and outside spaces (Figure 1) of the materials can be followed by NMR. The observed OH/NH ratios provide insight into the pore filling mechanisms. From the data analysis, surface/volume, volume/volume, and surface/surface ratios of the different spaces can be derived.

(ii) The HGPE NMR tool is useful for the study of the structures of porous solids in molecular dimensions, which complements the traditional tools[1−6] described in the Introduction. By contrast, diffusion NMR represents an important tool for the study of microscopic structures.[8]

(iii) We have found that the volumes of the external void spaces of the MCM-41 and SBA-15 samples studied are larger than those of the internal pores. On the other hand, the surface areas of the external spaces are much smaller than those of the internal pores in the case of the MCM-41 sample, whereas the difference is much less pronounced in the case of SBA-15.

(iv) The filling of the internal pores of the mesoporous silica samples with the guest molecules such as 4-methyl-1*H*-pyrazole (MPz) seems to proceed after the formation of a submonolayer in an inhomogeneous way with the coexistence of filled and void pore segments. First, guest molecules only enter the internal pores but at larger filling ratios more guests are found in the external spaces, although the internal pores are not yet full. For SBA-15, the irregular internal surface observed previously[39] will increase the inhomogeneity of the guest filling in such a way that the difference with the external cavities is alleviated.

(v) Estimates of the number of MPz molecules and their relative size with respect to the surface features, ideas about their hydrogen-bonded structure, and proton exchange mechanisms in the internal pores are presented. These ideas might provide a guideline for future molecular simulations of hydrogen-bonded guest−host interactions.

(vi) Many open questions remain, among which are whether MAS techniques are compulsory or whether also static samples could be measured, whether MAS decreases the external volumes strongly, whether the results depend on temperature, whether the samples studied are representative for all samples of the same type, whether there is an influence of the type and shape of the crystallites, whether the internal/external surface and volume ratios can be modeled, and whether guest exchange between different spaces can be characterized. These and other open questions could not be studied at present, where we focus on the method but may constitute a fruitful research area in the future.

ASSOCIATED CONTENT

Supporting Information

The Supporting Information is available free of charge at https://pubs.acs.org/doi/10.1021/acs.jpcc.0c04889.

Composition of 4-methyl-1*H*-pyrazole (MPz) inside silica of the MCM-41 type and ^{1}H MAS chemical shifts δ at 398 K (Table S1); composition of 4-methyl-1*H*-pyrazole (MPz) inside silica of the SBA-15 type and ^{1}H MAS chemical shifts δ at 398 K (Table S2); selected single 90° pulse ^{1}H MAS NMR spectra at 398 K and 7 T of 4-methyl-1*H*-pyrazole in MCM-41 (Figure S1);

https://dx.doi.org/10.1021/acs.jpcc.0c04889
J. Phys. Chem. C 2020, 124, 22082−22095

selected single 90° pulse ^{1}H MAS NMR spectra at 398 K and 7 T of 4-methyl-1*H*-pyrazole in SBA-15 (Figure S2); and density of neat 4-methyl-1*H*-pyrazole at different temperatures according to the data of Table 3 (Figure S3) (PDF)

AUTHOR INFORMATION

Corresponding Authors

Ilya G. Shenderovich − *Faculty of Chemistry and Pharmacy, University of Regensburg, 93053 Regensburg, Germany;* orcid.org/0000-0001-6713-9080; Email: Ilya.Shenderovich@chemie.uni-regensburg.de

Hans-Heinrich Limbach − *Institut für Chemie und Biochemie, Freie Universität Berlin, 14195 Berlin, Germany;* orcid.org/0000-0002-2084-6359; Email: limbach@chemie.fu-berlin.de

Authors

Verónica Torres-Barthelemy − *Institut für Chemie und Biochemie, Freie Universität Berlin, 14195 Berlin, Germany*

Natalia Pérez-Hernández − *Institut für Chemie und Biochemie, Freie Universität Berlin, 14195 Berlin, Germany; Institute for Chemical Research (CSIC-US), E-41092 Seville, Spain*

Peter M. Tolstoy − *St. Petersburg State University, 198504 St. Petersburg, Russian Federation;* orcid.org/0000-0002-8426-3988

Gleb S. Denisov − *Department of Physics, St. Petersburg State University, 198504 St. Petersburg, Russian Federation;* orcid.org/0000-0002-1246-0552

Complete contact information is available at: https://pubs.acs.org/10.1021/acs.jpcc.0c04889

Notes

The authors declare no competing financial interest.

ACKNOWLEDGMENTS

We are indebted to the late Prof. Dr. Gerhard Findenegg for many stimulating discussions and his co-worker Dr. Dilek Akcakayiran for providing us with samples of MCM-41 and SBA-15. We also thank Prof. Dr. Gerd Buntkowsky, Darmstadt, for many helpful discussions during our common work on mesoporous silica materials. This work has been supported by the Freie Universität Berlin and the Deutsche Forschungsgemeinschaft, Bonn (SFB 448 TP B2).

REFERENCES

(1) Lowell, S.; Shields, J. E.; Thomas, M. A.; Thommes, M. *Characterization of Porous Solids and Powders: Surface Area, Pore Size and Density*; Kluwer Academic Publishers: Dordrecht, The Netherlands, 2004.

(2) Klobes, P.; Meyer, K.; Munro, R. G. *Porosity and Specific Surface Area*, Special Publication 960-17; National Institute of Standards and Technology, 2006; pp 1−89.

(3) Brunauer, S.; Emmett, P. H.; Teller, E. Adsorption of Gases in Multimolecular Layers. *J. Am. Chem. Soc.* **1938**, *60*, 309−319.

(4) Sayari, A.; Liu, P.; Kruk, M.; Jaroniec, M. Characterization of Large-Pore MCM-41 Molecular Sieves Obtained via Hydrothermal Restructuring. *Chem. Mater.* **1997**, *9*, 2499−2506.

(5) Webb, P. A. *An Introduction to the Physical Characterization of Materials by Mercury Intrusion Porosimetry with Emphasis on Reduction and Presentation of Experimental Data*; Micromeritics Instrument Corp.: Norcross, Georgia, 2001; pp 1−23. https://www.micromeritics.com/pdf/app_articles/mercury_paper.pdf.

(6) Webb, P. A. *Volume and Density Determinations for Particle Technologists*; Micromeritics Instrument Corp.: Norcross, Georgia, 2001; pp. 1−15. https://www.micromeritics.com/Repository/Files/Volume_and_Density_determinations_for_Particle_Technologists.pdf.

(7) Mair, R. W.; Wong, G. P.; Hoffmann, D.; Hürlimann, M. D.; Patz, S.; Schwartz, L. M.; Walsworth, R. L. Probing Porous Media with Gas Diffusion NMR. *Phys. Rev. Lett.* **1999**, *83*, 3324−3327.

(8) Hürlimann, M. D.; Helmer, K. G.; Latour, L. L.; Sotak, C. H. Restricted Diffusion in Sedimentary Rocks. Determination of Surface-Area-to-volume Ratio and Surface Relaxivity. *J. Magn. Reson., Ser. A* **1994**, *111*, 169−178.

(9) Hollenbach, J.; Anger, B. In *Diffusion NMR of Confined Systems: Fluid Transport in Porous Solids and Heterogeneous Materials*; Valiullin, R., Eds.; New Developments in NMR; Royal Society of Chemistry, 2017; Vol. 9, pp 294−317.

(10) Auwers, K. v.; Cauer, E. Über Acyl-pyrazole. *J. Prakt. Chem.* **1930**, *126*, 146−176.

(11) Aguilar-Parrilla, F.; Klein, O.; Elguero, J.; Limbach, H. H. A Dynamic ^{15}N NMR Study of Kinetic Hydrogen/Deuterium Isotope and Tunnel Effects on the Triple Proton Transfer in Crystalline 3,5-Dimethylpyrazole. *Ber. Bunsenges. Phys. Chem.* **1997**, *101*, 889−901.

(12) Klein, O.; Aguilar-Parrilla, F.; López del Amo, J. M.; Jagerovic, N.; Elguero, J.; Limbach, H. H. Dynamic NMR Study of the Mechanisms of Double, Triple and Quadruple Proton and Deuteron Transfer in Cyclic Hydrogen Bonded Solids of Pyrazole Derivatives. *J. Am. Chem. Soc.* **2004**, *126*, 11718−11732.

(13) Aguilar-Parrilla, F.; Cativiela, C.; Diaz de Villegas, M. D.; Elguero, J.; Foces-Foces, C.; Laureiro, J. I. G.; Cano, F. H.; Limbach, H. H.; Smith, J. A. S.; Toiron, C. The Tautomerism of 3(5)-Phenylpyrazoles: An Experimental (^{1}H,^{13}C, ^{15}N NMR and X-Ray Crystallography) and Theoretical (STO-3G) Study. *J. Chem. Soc., Perkin 2* **1992**, 1737−1742.

(14) Toda, F.; Tanaka, K.; Foces-Foces, C.; Llamas-Saiz, A. L.; Limbach, H. H.; Aguilar-Parrilla, F.; Claramunt, R. M.; Lopez, C.; Elguero, J. Intermolecular Proton Transfer in Host-Guest Crystals: the Case of Pyrazole Included in 1,1-Di(2,4-dimethylphenyl)but-2-yn-1-ol, an X-Ray and Solid State ^{13}C/^{15}N NMR Study. *J. Chem. Soc., Chem. Commun.* **1993**, 1139−1142.

(15) Becker, N. N.; Roberts, J. D. Structure of the Liver Alcohol Dehydrogenase-NAD^{+}-Pyrazole Complex As Determined by ^{15}N NMR Spectroscopy. *Biochemistry* **1984**, *23*, 3336−3340.

(16) Goddard, R.; Claramunt, R. M.; Escolástico, C.; Elguero, J. Structures of NH-pyrazoles bearing only C-methyl substituents: 4-methylpyrazole is a hydrogen-bonded trimer in the solid (100 K). *New J. Chem.* **1999**, *23*, 237−240.

(17) Monkhouse, D. C.; Lach, J. L. Use of adsorbents in enhancement of drug dissolution II. *J. Pharm. Sci.* **1972**, *61*, 1435−1441.

(18) Yang, K. A.; Glemza, R.; Jarowski, C. I. Effects of amorphous silicon dioxides on drug dissolution. *J. Pharm. Sci.* **1979**, *68*, 560−565.

(19) Beck, J. S.; Vartuli, J. C.; Roth, W. J.; Leonowicz, M. E.; Kresge, C. T.; Schmitt, K. D.; Chu, C. T. W.; Olson, D. H.; Sheppard, E. W.; McCullen, S. B.; Higgins, J. B.; Schlenker, J. L. A New Family of Mesoporous Molecular Sieves Prepared with Liquid Crystal Templates. *J. Am. Chem. Soc.* **1992**, *114*, 10834−10843.

(20) Zhao, D.; Feng, J.; Huo, Q.; Melosh, N.; Fredrickson, G. H.; Chmelka, B. F.; Stucky, G. D. Triblock Copolymer Syntheses of Mesoporous Silica with Periodic 50 to 300 Angstrom Pores. *Science* **1998**, *279*, 548−552.

(21) Rimola, A.; Costa, D.; Sodupe, M.; Lambert, J. F.; Ugliengo, P. Silica Surface Features and Their Role in the Adsorption of Biomolecules: Computational Modeling and Experiments. *Chem. Rev.* **2013**, *113*, 4216−4313.

(22) Muñoz, B.; Rámila, A.; Pérez-Pariente, J.; Díaz, I.; Vallet-Regí, M. MCM-41 Organic Modification as Drug Delivery Rate Regulator. *Chem. Mater.* **2003**, *15*, 500−503.

(23) Tao, S. L.; Desai, T. A. Microfabricated drug delivery systems: from particles to pores. *Adv. Drug Delivery Rev.* **2003**, *55*, 315−328.

(24) Slowing, I. I.; Vivero-Escoto, J. L.; Wu, C. W.; Lin, V. S. Mesoporous silica nanoparticles as controlled release drug delivery

and gene transfection carriers. *Adv. Drug Delivery Rev.* **2008**, *60*, 1278−1288.
(25) Melde, B. J.; Johnson, B. J.; Charles, P. T. Mesoporous Silicate Materials in Sensing. *Sensors* **2008**, *8*, 5202−5228.
(26) Taguchi, A.; Schüth, F. Ordered mesoporous materials in catalysis. *Microporous Mesoporous Mater.* **2005**, *77*, 1−45.
(27) Srour, M.; Hadjiali, S.; Sauer, G.; Brunnengräber, K.; Breitzke, H.; Xu, Y.; Weidler, H.; Limbach, H. H.; Gutmann, T.; Buntkowsky, G. Synthesis and solid-state NMR characterization of a novel, robust, pyridyl-based immobilized Wilkinson's type catalyst with high catalytic performance. *ChemCatChem* **2016**, *8*, 3409−3416.
(28) Webb, J. D.; Seki, D.; Goldston, J. F.; Pruski, M.; Crudden, C. M. Selective Functionalization of the Mesopores of SBA−15. *Microporous Mesoporous Mater.* **2015**, *203*, 123−131.
(29) Vinu, A.; Miyahara, M.; Ariga, K. Assemblies of Biomaterials in Mesoporous Media. *J. Nanosci. Nanotechnol.* **2006**, *6*, 1510−1532.
(30) Cavalleri, M.; Hermann, K.; Knop-Gericke, A.; Hävecker, M.; Herbert, R.; Hess, C.; Oestereich, A.; Döbler, J.; Schlögl, R. Analysis of silica-supported vanadia by X-ray absorption spectroscopy: Combined theoretical and experimental studies. *J. Catal.* **2009**, *262*, 215−223.
(31) Solovyov, L. A.; Kirik, S. D.; Shmakov, A. N.; Romannikov, V. N. X-ray structural modeling of silicate mesoporous mesophase material. *Microporous Mesoporous Mater.* **2001**, *44*−*45*, 17−23.
(32) Schacht, S.; Janicke, M.; Schüth, S. Modeling X-ray patterns and TEM images of MCM-41. *Microporous Mesoporous Mater.* **1998**, *22*, 485−493.
(33) Sauer, J.; Marlow, F.; Schüth, F. Simulation of powder diffraction patterns of modified ordered mesoporous materials. *Phys. Chem. Chem. Phys.* **2001**, *3*, 5579−5584.
(34) Edler, K. J.; Reynolds, P. A.; White, J. W. Small-Angle Neutron Scattering Studies on the Mesoporous Molecular Sieve MCM-41. *J. Phys. Chem. B* **1998**, *102*, 3676−3683.
(35) Schreiber, A.; Ketelsen, I.; Findenegg, G. H. Melting and freezing of water in ordered mesoporous silica materials. *Phys. Chem. Chem. Phys.* **2001**, *3*, 1185−1195.
(36) Müter, D.; Shin, T.; Demé, B.; Fratzl, P.; Paris, O.; Findenegg, G. H. Surfactant Self-Assembly in Cylindrical Silica Nanopores. *J. Phys. Chem. Lett.* **2010**, *1*, 1442−1446.
(37) Balzer, C.; Waag, A. M.; Gehret, S.; Reichenauer, G.; Putz, F.; Huesing, N.; Paris, O.; Bernstein, N.; Gor, G. I.; Neimark, A. V. Adsorption-Induced Deformation of Hierarchically Structured Mesoporous Silica-Effect of Pore-Level Anisotropy. *Langmuir* **2017**, *33*, 5592−5602.
(38) Balzer, C.; Waag, A. M.; Putz, F.; Huesing, N.; Paris, O.; Gor, G. I.; Neimark, A. V.; Reichenauer, G. Mechanical Characterization of Hierarchical Structured Porous Silica by in Situ Dilatometry Measurements during Gas Adsorption. *Langmuir* **2019**, *35*, 2948−2956.
(39) Shenderovich, I. G.; Buntkowsky, G.; Schreiber, A.; Gedat, E.; Sharif, S.; Albrecht, J.; Golubev, N. S.; Findenegg, G. H.; Limbach, H. H. Pyridine-^{15}N - a Mobile NMR Sensor for Surface Acidity and Surface Defects of Mesoporous Silica. *J. Phys. Chem. B* **2003**, *107*, 11924−11939.
(40) Shenderovich, I. G.; Mauder, D.; Akcakayiran, D.; Buntkowsky, G.; Limbach, H. H.; Findennegg, G. H. NMR Provides Checklist of Generic Properties for Atomic-Scale Models of Periodic Mesoporous Silicas. *J. Phys. Chem. B* **2007**, *111*, 12088−12096.
(41) Buntkowsky, G.; Vogel, M. Zeitschrift für Physikalische Chemie Special Issue: Research Unit FOR 1583: Hydrogen-Bonded Liquids Subject to Interfaces of Various Hydroaffinities. *Z. Phys. Chem.* **2018**, *232*, 935−1261.
(42) Zhao, X. S.; Lu, G. O.; Whittaker, A. K.; Millar, G. J.; Zhu, H. Y. Comprehensive Study of Surface Chemistry of MCM-41 Using ^{29}Si CP/MAS NMR, FTIR, Pyridine-TPD, and TGA. *J. Phys. Chem. B* **1997**, *101*, 6525−6531.
(43) Cheng, C. F.; Zhou, W.; Park, D. H.; Klinowski, J.; Hargreaves, M.; Gladden, L. F. Controlling the channel diameter of the mesoporous molecular sieve MCM-41. *J. Chem. Soc., Faraday Trans.* **1997**, *93*, 359−363.
(44) Trébosc, J.; Wiench, J. W.; Huh, S.; Lin, V. S. Y.; Pruski, M. Solid-State NMR Study of MCM-41-type Mesoporous Silica Nanoparticles. *J. Am. Chem. Soc.* **2005**, *127*, 3057−3068.
(45) Ip, B. C. K.; Andreeva, D. V.; Buntkowsky, G.; Akcakayiran, D.; Findenegg, G. H.; Shenderovich, I. G. NMR study of proton transfer to strong bases on inner surfaces of MCM-41. *Microporous Mesoporous Mater.* **2010**, *134*, 22−28.
(46) Nossov, A.; Haddad, E.; Guenneau, F.; Galarneau, A.; Di Renzo, F.; Fajula, F.; Gédéon, A. Characterization of the Porosity in SBA-15 Silicas by Hyperpolarized ^{129}Xe NMR. *J. Phys. Chem. B* **2003**, *107*, 12456−12460.
(47) Buntkowsky, G.; Breitzke, H.; Adamczyk, A.; Roelofs, F.; Emmler, T.; Gedat, E.; Grünberg, B.; Xu, Y.; Limbach, H. H.; Shenderovich, I. G.; Vyalikh, A.; Findenegg, G. Structural and dynamical properties of guest molecules confined in mesoporous silica materials revealed by NMR. *Phys. Chem. Chem. Phys.* **2007**, *9*, 4843−4853.
(48) Grünberg, B.; Emmler, T.; Gedat, E.; Shenderovich, I. G.; Findenegg, G. H.; Limbach, H. H.; Buntkowsky, G. Hydrogen Bonding of Water confined in mesoporous Silica MCM-41 and SBA-15 studied by ^{1}H-Solid State NMR. *Chem. − Eur. J.* **2004**, *10*, 5689−5696.
(49) Mauder, D.; Akcakayiran, D.; Lesnichin, S. B.; Findenegg, G. H.; Shenderovich, I. G. Acidity of Sulfonic and Phosphonic Acid-Functionalized SBA-15 under Almost Water-Free Conditions. *J. Phys. Chem. C* **2009**, *113*, 19185−19192.
(50) Gedat, E.; Schreiber, A.; Albrecht, J.; Emmler, Th.; Shenderovich, I.; Findenegg, G. H.; Limbach, H. H.; Buntkowsky, G. Evidence for surface and core phases of benzene-d_6 confined in mesoporous silica SBA-15 as studied with ^{2}H-NMR. *J. Phys. Chem. B* **2002**, *106*, 1977−1984.
(51) Harrach, M. F.; Drossel, B.; Winschel, W.; Gutmann, T.; Buntkowsky, G. Mixtures of Isobutyric Acid and Water Confined in Cylindrical Silica Nanopores Revisited: A Combined Solid-State NMR and Molecular Dynamics Simulation Study. *J. Phys. Chem. C* **2015**, *119*, 28961−28969.
(52) Kumari, B.; Brodrecht, M.; Breitzke, H.; Werner, M.; Grünberg, B.; Limbach, H. H.; Forg, S.; Sanjon, E.; Drossel, B.; Gutmann, T.; Buntkowsky, G. Mixtures of Alcohols and Water Confined in Mesoporous Silica- a Combined Solid-State NMR and Molecular Dynamic Simulation Study. *J. Phys. Chem. C* **2018**, *122*, 19540−19550.
(53) Weigler, M.; Brodrecht, M.; Buntkowsky, G.; Vogel, M. Reorientation of Deeply Cooled Water zn Mesoporous Silica: NMR Studies of the Pore-Size Dependence. *J. Phys. Chem. B* **2019**, *123*, 2123−2134.
(54) Dosseh, G.; Xia, Y.; Alba-Simionesco, C. Cyclohexane and benzene confined in MCM-41 and SBA-15: confinement effects on freezing and melting. *J. Phys. Chem. B* **2003**, *107*, 6445−6453.
(55) Lusceac, S. A.; Koplin, C.; Medick, P.; Vogel, M.; Brodie-Linder, N.; LeQuellec, C.; Alba-Simionesco, C.; Roessler, E. A. Type A versus type B glass formers: NMR relaxation in bulk and confining geometry. *J. Phys. Chem. B* **2004**, *108*, 16601−16605.
(56) Alba-Simionesco, C.; Coasne, B.; Dosseh, G.; Dudziak, G.; Gubbins, K.; Radhakrishnan, R.; Sliwinska-Bartkowiak, M. Effects of Confinement on Freezing and Melting. *J. Phys.: Condens. Matter* **2006**, *18*, R15−R68.
(57) Mafra, L.; Čendak, T.; Schneider, S.; Wiper, P. V.; Pires, J.; Gomes, J. R. B.; Pinto, M. L. Structure of Chemisorbed CO_2 Species in Amine-Functionalized Mesoporous Silicas Studied by Solid-State NMR and Computer Modeling. *J. Am. Chem. Soc.* **2017**, *139*, 389−408.
(58) Lesage, A.; Lelli, M.; Gajan, D.; Caporini, M. A.; Vitzthum, V.; Mieville, P.; Alauzun, J.; Roussey, A.; Thieuleux, C.; Mehdi, A.; Bodenhausen, G.; Coperet, C.; Emsley, L. Surface Enhanced NMR Spectroscopy by Dynamic Nuclear Polarization. *J. Am. Chem. Soc.* **2010**, *132*, 15459−15461.

https://dx.doi.org/10.1021/acs.jpcc.0c04889
J. Phys. Chem. C 2020, 124, 22082−22095

(59) Lafon, O.; Thankamony, A. S. L.; Kobayashi, T.; Carnevale, D.; Vitzthum, V.; Slowing, I. G.; Kandel, K.; Vezin, H.; Amoureux, J. P.; Bodenhausen, G.; Pruski, M. Mesoporous Silica Nanoparticles Loaded with Surfactant: Low Temperature Magic Angle Spinning ^{13}C and ^{29}Si NMR Enhanced by Dynamic Nuclear Polarization. *J. Phys. Chem. C* **2013**, *117*, 1375−1382.
(60) Kobayashi, T.; Pruski, M. Spatial Distribution of Silica-Bound Catalytic Organic Functional Groups Can Now Be Revealed by Conventional and DNP-Enhanced Solid-State NMR Methods. *ACS Catal.* **2019**, *9*, 7238−7249.
(61) Ruth, A. A.; Lesche, H.; Nickel, B. Temperature Dependence of Viscosity and Density of cis-1,4/trans-1,3-Dimethylcyclohexane and Several other Commonly Used Organic Solvents. *Z. Phys. Chem.* **2003**, *217*, 707−722.
(62) De Boer, J. H. Untersuchungen über mikroporöse Salz- und Oxyd-Systeme. *Angew. Chem.* **1958**, *70*, 383−389.
(63) Akcakayiran, D.; Mauder, D.; Hess, C.; Sievers, T. K.; Kurth, D. G.; Shenderovich, I. G.; Limbach, H. H.; Findenegg, G. H. Carboxylic Acid-Doped SBA-15 Silica as a Host for Metallo-supramolecular Coordination Polymers. *J. Phys. Chem. B* **2008**, *112*, 14637−14647.
(64) Gurinov, A. A.; Rozhkova, Y. A.; Zukal, A.; Čejka, J.; Shenderovich, I. G. Mutable Lewis and Brønsted Acidity of Aluminated SBA-15 as Revealed by NMR of Adsorbed Pyridine-^{15}N. *Langmuir* **2011**, *27*, 12115−12123.
(65) Vyalikh, A.; Emmler, Th.; Shenderovich, I.; Zeng, Y.; Findenegg, G. H.; Buntkowsky, G. ^{2}H-Solid State NMR and DSC Study of Isobutyric Acid in Mesoporous Silica Materials. *Phys. Chem. Chem. Phys.* **2007**, *9*, 2249−2257.
(66) Foces-Foces, C.; Echevarría, A.; Jagerovic, N.; Alkorta, I.; Elguero, J.; Langer, U.; Klein, O.; Minguet-Bonvehí, M.; Limbach, H. H. A Solid State NMR, X-Ray Diffraction and *Ab initio* Computational Study of Hydrogen Bond Structure and Dynamics of Pyrazole-4-Carboxylic Acid Chains. *J. Am. Chem. Soc.* **2001**, *123*, 7898−7906.
(67) Limbach, H. H.; Männle, F.; Denisov, G. S.; Detering, C. Dynamic NMR studies of base-catalyzed intramolecular single vs. intermolecular double proton transfer of 1,3-bis(4-fluorophenyl)-triazene. *Chem. Phys.* **2005**, *319*, 69−92.
(68) Buntkowsky, G.; Vogel, M.; Winter, R. Properties of Hydrogen-Bonded Liquids at Interfaces. *Z. Phys. Chem.* **2018**, *232*, 937−972.

https://dx.doi.org/10.1021/acs.jpcc.0c04889
J. Phys. Chem. C 2020, 124, 22082−22095